Materials Advances

ROYAL SOCIETY OF CHEMISTRY

PAPER

View Article Online
View Journal | View Issue

Cite this: *Mater. Adv.*, 2025, 6, 4337

Enhanced electrochemical performance of S,N-containing carbon materials derived from covalent triazine-based frameworks with a tetrathiafulvalene core†

Arijit Maity,[a] Anupam Jana,[a] Sandeep Kumar Dey,[b] Christoph Janiak *[c] and Asamanjoy Bhunia *[a]

To address the challenges posed by a growing population, limited resources, and demands of modern lifestyles, energy research is of prime importance. In this context, we have used 2,3,6,7-tetra(4-cyanophenyl)tetrathiafulvalene (TTFCN), a redox-active building block, to fabricate a pair of covalent triazine-based frameworks (CTFs), named CTFTTF@1-400 and CTFTTF@2-400 (where 1 = $ZnCl_2$: monomer (5 : 1); 2 = $ZnCl_2$: monomer (10 : 1)) under Lewis acidic ($ZnCl_2$) conditions at 400 °C for supercapacitor applications. To enhance the supercapacitor performance of CTFs, we have carried out the synthesis at 700 °C, resulting in the formation of the S,N-containing carbon material CTFTTF@2-700. Nitrogen sorption isotherms (77 K) revealed BET surface areas of 330, 650 and 1350 $m^2\ g^{-1}$ for CTFTTF@1-400, CTFTTF@2-400, and CTFTTF@2-700, respectively, with different micropore to mesopore ratios. These porous materials when used as electrodes, specifically CTFTTF@2-700 exhibited an excellent electrochemical performance with the highest specific capacitance of 943 F g^{-1} at 1 A g^{-1} and 708 F g^{-1} at 1 A g^{-1} in a three-electrode system and a two-electrode system, respectively, which was superior to that of most analogous materials reported previously. Additionally, it also demonstrated excellent cyclic stability, retaining 90% of its capacitance after 10 000 cycles in a three-electrode system using a 1 mol L^{-1} Na_2SO_4 electrolyte. The high supercapacitor performance of CTFTTF@2-700 can be attributed to its high specific surface area, optimal micropore-to-mesopore ratio and significant content of heteroatoms, specifically sulfur and nitrogen.

Received 13th March 2025,
Accepted 8th May 2025

DOI: 10.1039/d5ma00225g

rsc.li/materials-advances

Introduction

Use of renewable energy technologies such as solar and wind is increasing. This leads to a growing need for high-capacity energy storage systems, as they play a vital role in balancing energy fluctuations, optimizing distribution, and enabling flexible deployment.[1,2] Among various energy storage systems, electrochemical supercapacitors (ESCs) have gained significant attention in recent years. This is due to their remarkable features, such as high power density, fast charging/discharging capability, wide operating temperature range, extended cycle life, excellent processability, and superior electrical conductivity.[3] These advantageous characteristics position supercapacitors (SCs) as an ideal choice for high-power applications, including high-speed transportation and technologies that demand rapid on–off responses. Examples include uninterruptible power supplies, hybrid electric vehicles, grid stabilization systems, forklifts, load cranes, military systems, aerospace equipment and more. SCs offer distinct advantages over batteries, such as faster charging and discharging rates and higher power density. Their quick charge and discharge capabilities enable SCs to recover excess kinetic energy when vehicles or large machinery slow down or stop, a process that requires much higher current levels than batteries can provide.[4] As a result, large-capacity energy storage systems based on SCs have seen continuous development in recent years. The global SC industry market size grew from $1.82 billion in 2022 to $2.02 billion in 2023 and to $2.94 billion by 2024.

Unlike conventional capacitors, supercapacitors store charge *via* either faradaic or non-faradaic processes.[5–7] Pseudocapacitors, a type of supercapacitor, store charge through faradaic processes involving reversible redox reactions at the electrode surface, which facilitate rapid electron and charge transfer between the electrode and electrolyte.[8] In the non-faradaic

[a] *Department of Chemistry, Inorganic Chemistry Section, Jadavpur University, Kolkata, 700032, India. E-mail: abhunia.chemistry@jadavpuruniversity.in*
[b] *Material Science and Technology Division, CSIR-North East Institute of Science and Technology, Jorhat, Assam 785006, India*
[c] *Institut für Anorganische Chemie und Strukturchemie, Heinrich-Heine-Universität Düsseldorf, 40204 Düsseldorf, Germany*

† Electronic supplementary information (ESI) available: Synthesis of ligand (TTFCN), IR, CHN, TGA, supercapacitive energy storage details, and comparison table of capacitance values. See DOI: https://doi.org/10.1039/d5ma00225g

process, energy storage takes place *via* an electrical double-layer capacitance mechanism, where charge is stored through the reversible adsorption and desorption of electrolyte ions at the interfaces between the electrode and electrolyte.[9] Therefore, in both cases, materials with a substantial active surface area and high porosity are essential for enhancing the performance of ESCs. The pursuit of improving ESCs or ESC's performance is closely linked to the investigation of novel electrodes. To date, various porous carbon nanostructures, such as activated carbon, porous graphene, graphene aerogel, mesoporous carbon, and other carbon-based materials, have been developed for high-performance capacitors.[10–12] However, the carbon materials used in SC electrodes have several critical limitations, including low energy and power densities, shorter charge–discharge cycles, lower recyclability, *etc.*[13] These issues can hinder the overall effectiveness and sustainability of supercapacitors in energy storage applications. To overcome these challenges, two research efforts have garnered significant attention in recent years, the heteroatom effect (HAE)[14] and the micropore effect (MPE)[15] introduced into porous carbon structures. Additionally, other porous materials including metal–organic frameworks (MOFs),[16] conjugated microporous materials (CMPs),[17] covalent-organic frameworks (COFs)[2] and covalent triazine-based frameworks (CTFs)[18] demonstrate significant potential as effective electrodes for enhancing the efficiency of ESCs. Among them, CTFs have become a popular choice for energy storage materials due to their high inherent nitrogen content and adjustable porosity, which improve electrochemical performance by influencing electron diffusion kinetics and distribution within the carbon network. The robust triazine units in CTFs enhance their durability, reducing the likelihood of degradation during electrochemical reactions. In this context, several N-containing carbon materials derived from CTFs have been synthesized for supercapacitors. Yang *et al.* and Kuo *et al.* reported nitrogen-doped CTFs, p-CTF-800[19] and Car-CTF,[20] with capacitance values of 406 F g^{-1} and 545 F g^{-1}, respectively. Recently, we have also reported the performance of bipolar supercapacitors utilizing pyridine-based carbon materials derived from CTFs.[21] In the negative potential window, the material demonstrated a specific capacitance of 435 F g^{-1} (at 1 A g^{-1}), which was significantly higher than the specific capacitance of 306 F g^{-1} (at 1 A g^{-1}) observed in the positive potential window. In the previous study, it has been observed that a nitrogen-induced heteroatom effect can significantly improve the supercapacitor performance of porous materials. This concept was effectively applied in imine-based COF materials using a donor–acceptor approach. In 2023, Pachfule and coworkers reported a COF featuring dithiophenedione moieties in its backbone (TTT-DHTD), which showed a capacitance of 273 F g^{-1} at a charge–discharge rate of 0.5 A g^{-1}.[22] Two other groups, Tan *et al.* and Yang *et al.*, developed sulfur-based COFs, specifically NDTT[23] and DBT-MA-COF,[24] which demonstrated capacitance values of 425.3 F g^{-1} and 407 F g^{-1}, respectively. To the best of our knowledge, sulfur-based CTF materials have not been previously reported for supercapacitor applications.[25]

Herein, we introduce, for the first time, the thiafulvalene-based ligand 2,3,6,7-tetra(4-cyanophenyl)tetrathiafulvalene (TTFCN) for synthesizing CTF materials that combine electron-rich thiafulvalene moieties with electron-accepting triazine rings. A trimerization reaction of the nitrile groups in TTFCN can effectively promote the formation of CTF materials, using $ZnCl_2$ as both a Lewis acid and a solvent (porogen) at 400 °C. By employing a higher temperature of 700 °C, the CTF materials undergo a transformation into sulfur- and nitrogen-containing carbon materials, designated as CTFTTF@2-700. The electrochemical performance indicated that CTFTTF@2-700 exhibited a specific capacitance of 943 F g^{-1} at 1 A g^{-1} and demonstrated excellent electrochemical cycling stability throughout the cycling process.

Experimental section

Materials

All chemicals were purchased from commercial suppliers (Sigma-Aldrich, Acros Organics, and TCI chemical company) and used without further purification.

Analytical techniques

Infrared (IR) spectra were obtained on a Bruker FT-IR Tensor 37 spectrometer in the 4000–550 cm^{-1} region with 2 cm^{-1} resolution as KBr disks. NMR experiments were performed on Bruker DPX300 spectrometers at 298 K. The manufacturers' supplied Bruker TopSpin 3.6.2 software was utilized to process the data. NMR chemical shifts were recorded in δ ppm by locking and calibration with appropriate deuterated NMR solvents. Elemental analyses were carried out using a PerkinElmer 2400 series II elemental analyzer. Powder X-ray diffraction (PXRD) data were collected on a Bruker D2 Phaser diffractometer using a flat sample holder, including flat silicon, low background sample holder, and Cu $K\alpha_1/\alpha_2$ radiation with λ = 1.5418 Å at 30 kV covering 2theta angles 5–80° over a time of 2 h (0.01° sec^{-1}). Diffractograms were obtained on flat layer sample holders where at a low angle the beam spot is strongly broadened so that only a fraction of the reflected radiation reaches the detector which leads to low relative intensities measured at $2\theta < 7°$. For hygroscopic or air-sensitive samples, the sample holder can be sealed with a dome. Scanning electron microscopy (SEM) images were obtained using an ESEM Quanta 400 FEG SEM equipped with a secondary electron detector. Thermogravimetric analyses (TGA) were carried out at a ramp rate of 10 °C min^{-1} under N_2 flow with a Netzsch TG 209 F3 Tarsus. Nitrogen physisorption isotherms were carried out on a Nova 4000e from Quantachrome at 77 K (liquid nitrogen bath) using N_2 gas of 99.99% purity. The sample was connected to the preparation port of the sorption analyzer and degassed under vacuum until the outgassing rate, *i.e.*, the rate of pressure rises in the temporarily closed manifold with the connected sample tube, was less than 2 μTorr min^{-1} at a specified temperature of 130 °C. After weighing, the sample tube was then transferred to the analysis port of the sorption analyzer. Helium gas was used for the determination of the cold and warm free space of the sample tubes. The DFT pore size distributions ('N_2 DFT slit pore' model) were calculated using the NovaWin 11.03' software. X-ray photoelectron spectroscopy (XPS) measurement was

conducted using the Thermo Fisher ESCALAB Xi+ microProbe instrument with a monochromatic Al–Kα target, 1486.6 eV energy, and a maximum power of 15.0 kW.

Electrochemical measurement was performed using a computerized CHI760E electrochemical workstation with a three-electrode system. Here, the counter electrode is the platinum electrode, the reference electrode is the Ag/AgCl electrode and the working electrode is the glassy carbon electrode immersed in 1 mol L^{-1} Na_2SO_4 solution as an electrolyte.

Synthesis of CTFs

CTFTTF@1-400 CTFTTF@2-400 and CTFTTF@2-700 were synthesized by following the procedure on CTF synthesis.[26–28]

CTFTTF@1-400

In a typical synthesis, an ampoule was charged with 2,3,6,7-tetra(4-cyanophenyl)tetrathiafulvalene (TTFCN) ligand (0.608 g, 1 mmol) and anhydrous $ZnCl_2$ (0.681 g, 5 mmol) under inert conditions. The ampoule was then flame sealed under vacuum. It was subsequently heated at 400 °C for 24 hours. After cooling to room temperature, the ampoule was carefully opened, and the black solid product was collected. This solid is washed thoroughly with deionized water (200 mL, three times), followed by diluted HCl (100 mL, three times). The residue was then washed with water (3 × 50 mL), tetrahydrofuran (3 × 50 mL), and acetone (3 × 50 mL), and finally dried under vacuum. Yield 58%.

CTFTTF@2-400

The same synthesis procedure was used as for CTFTTF@1-400 with a mixture of TTFCN (0.608 g, 1 mmol) and anhydrous $ZnCl_2$ (1.36 g, 10 mmol) heating to 400 °C under the ionothermal conditions for 33 h. Yield 62%.

CTFTTF@2-700

In a typical synthesis, a mixture of TTFCN (0.608 g, 1 mmol) and anhydrous $ZnCl_2$ (1.36 g, 10 mmol) was placed into a quartz ampoule under inert conditions. The quartz ampoule was then flame sealed under vacuum. The sealed ampoule was heated at 400 °C for 18 hours, followed by heating at 700 °C for an additional 15 hours. After cooling to room temperature, the ampoule was carefully opened, and the resulting black solid was collected. The solid was then washed by a previously established procedure. Yield 55%.

Preparation of CTF electrodes

The CTF electrode was prepared according to a previously reported procedure.[13] The CTF material (80 wt%) was blended with carbon black (10 wt%) and PVDF binder (10 wt%) in DMF. After stirring, the slurry was applied to a glassy carbon electrode and allowed to dry at room temperature for 12 hours.

Result and discussion

The CTFTTF materials were synthesized from 2,3,6,7-tetra(4-cyanophenyl)tetrathiafulvalene (TTFCN) *via* an ionothermal route in the presence of anhydrous $ZnCl_2$. $ZnCl_2$ served as a Lewis acid, molten solvent and porogen, facilitating the polymerization of TTFCN at temperatures ≥ 400 °C. Three CTFTTFs, named as CTFTTF@1-400, CTFTTF@2-400, CTFTTF@2-700, were obtained by varying the monomer to $ZnCl_2$ ratio, temperature and heating period (1 : 5, 400 °C and 24 h for CTFTTF@1-400, 1 : 10, 400 °C and 33 h for CTFTTF@2-400, 1 : 10, 400 °C for 18 h and 700 °C for 15 h for CTFTTF@2-700, respectively) (Scheme 1, and see the Experimental section for details). The applied reaction conditions yielded amorphous black solids with moderate to high surface areas and showing both micro- and mesoporous structures.

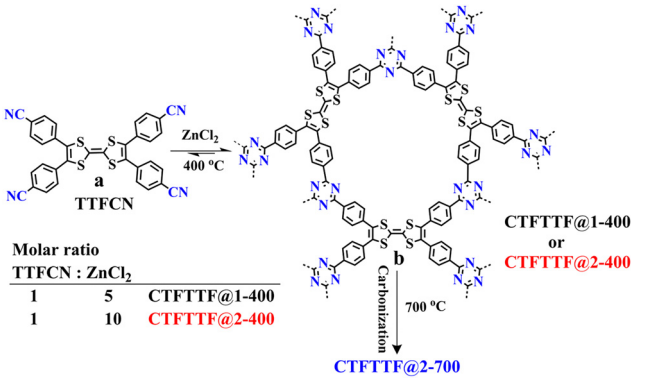

Scheme 1 (a) Structure of 2,3,6,7-tetra(4-cyanophenyl)tetrathiafulvalene (TTFCN). (b) Idealized structure of CTFTTF, which can be synthesized at 400 °C.

The FT-IR spectrum provided evidence for the formation of triazines and the consumption of the starting nitriles. The distinctive nitrile stretching band observed at approximately 2229 cm^{-1} was almost entirely diminished subsequent to the completion of the reaction (Fig. 1a and Fig. S1 in the ESI†).[29]

The signature bands associated with the triazine rings were observed in the ranges of 1360–1378 cm^{-1} (often very weak) and 1556–1595 cm^{-1}, corresponding to the C–N bending and stretching vibrations (Fig. 1a).[30,31] The crystallinity of the synthesized materials was assessed by powder X-ray diffraction (PXRD) technique. A broad peak at 24° (2θ) was detected in all the materials, signifying predominantly amorphous structures with some presence of graphitic two-dimensional layers (Fig. 1b).[32]

Moreover, a broad peak with low intensity for CTFTTF@2-700 was identified at approximately 44° (2θ), which corresponds to the diffraction pattern associated with the (111) basal plane of the diamond structure.[33] The thermal stability of the synthesized materials was examined by heating the activated samples up to 800 °C under a continuous flow of N_2 gas at the heating rate of 10 °C min^{-1}. Thermogravimetry analysis (TGA) showed that CTFTTF@1-400, CTFTTF@2-400 and CTFTTF@2-700 exhibited high thermal stability up to 500 °C (Fig. S2, ESI†). The porosity of these materials was evaluated by N_2 sorption measurements at 77 K. The adsorption isotherms of CTFTTF@1-400 and CTFTTF@2-400 exhibited a combination of type I(b) and type II isotherms (Fig. 1c). On the other hand, CTFTTF@2-700 displayed a type IV isotherm. When the relative pressure (P/P_0) exceeded approximately 0.8, the nitrogen uptake increased,

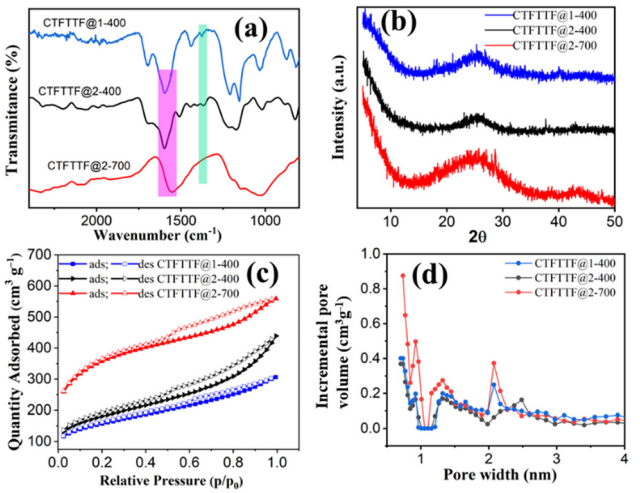

Fig. 1 (a) IR spectra, (b) PXRD, (c) N_2 sorption isotherms at 77 K, and (d) pore size distribution curves of CTFTTFs.

indicating a transition from micropore filling and monolayer adsorption to multilayer adsorption.[34,35] Moreover, a minor H4 hysteresis loop was observed for all the materials, indicative of capillary condensation occurring within mesoporous structures.[36] Nitrogen sorption isotherms (77 K) revealed BET specific surface areas of 330, 650 and 1350 $m^2\ g^{-1}$ for CTFTTF@1-400, CTFTTF@2-400 and CTFTTF@2-700, respectively (Table 1). These measurements clearly indicated that the surface area increased with a higher $ZnCl_2$ to monomer ratio and extended reaction time period.[30] Simultaneously, it was observed that the BET surface areas increased for materials synthesized at higher temperatures.[37] Pore size distributions were determined using non-local density functional theory (NLDFT) with the 'carbon slit pore' model. The CTFTTF materials exhibited a substantial proportion of micropores with diameters less than 2 nm (20 Å), reflecting their microporous nature (Fig. 1d). Additionally, a range of mesopores (20–30 Å) was identified, which could facilitate the transport of larger molecules. These pore characteristics were crucial for optimizing the performance of CTFTTFs in various applications. To evaluate the extent of microporosity in these materials, the ratio of micropore volume ($V_{0.1}$) to total pore volume (V_{tot}) was calculated based on N_2 sorption measurements (Table 1). The micropore/total pore volume ($V_{0.1}/V_{Total}$) was increased from 0.34 to 0.56 in the synthesized CTFTTFs. Scanning electron microscopy (SEM) analysis of the synthesized CTF materials revealed no distinct regular shape or size but showed the typical shard feature (Fig. 2, Fig. S3 and S4 in ESI†). Furthermore, transmission electron microscopy (TEM) was conducted to look a more detailed pore structural analysis of the CTF materials (Fig. S5, ESI†). The EDX was performed to identify the elemental composition of the material (Fig. S6 and S7, ESI†). The bonding characteristics of CTFTTF@2-400 and CTFTTF@2-700 were also examined using X-ray photoelectron spectroscopy (XPS) as depicted in Fig. 3.

The high-resolution C 1s spectrum of CTFTTF@2-400 was deconvoluted into three different peaks with binding energies of 284.7 eV, 286.08 eV, and 287.8 eV indicating C–N═C– in triazine units, C–C units, and oxidized C species, respectively (Fig. 3a).[38,39] Moreover, the high-resolution N 1s spectrum displayed three characteristic peaks at 398 eV, 399 eV, 400 eV. These peaks are attributed to pyridinic nitrogen in triazine rings (N═C), pyrrolic nitrogen and graphitic nitrogen (or quaternary), respectively (Fig. 3b).[40,41] The S 2p spectrum showed three distinctive peaks at 163.7 eV, 164.9 eV and 167.8 eV which are attributed to S═C, C–S–C and S═O units, respectively (Fig. 3c).[42,43] At the same time, the C 1s, N 1s and S 2p core-level spectra of CTFTTF@2-700 (Fig. 3d–f) are well matched with those of CTFTTF@2-400, which strongly suggests that both CTFs have similar types of carbon, nitrogen and sulfur atoms.[43,44] Additionally, quantitative XPS analysis of N 1s indicates that as the reaction temperatures are

Table 1 Porosity data for CTFTTF@1-400, CTFTTF@2-400 and CTFTTF@2-700

CTFs	S_{BET} ($m^2\ g^{-1}$)[a]	S_{Lang} ($m^2\ g^{-1}$)[b]	$V_{0.1}$ ($cm^3\ g^{-1}$)[c]	V_{Total} ($cm^3\ g^{-1}$)[d]	$V_{0.1}/V_{Total}$	Capacitance from GCD (F g^{-1}) at 1 A g^{-1}
CTFTTF@1-400	330	415	0.11	0.32	0.34	630
CTFTTF@2-400	650	806	0.24	0.68	0.35	808
CTFTTF@2-700	1350	1946	0.49	0.86	0.56	943

[a] Calculated BET surface area over the pressure range 0.01–0.05 P/P_0 from N_2 isotherms at 77 K. [b] Langmuir surface area over the pressure range 0–110 Torr. [c] Micropore volume calculated from N_2 adsorption isotherms at P/P_0 = 0.1 for pores ≤2 nm (20 Å). [d] Total pore volume at P/P_0 = 0.95 for pores ≤ 20 nm.

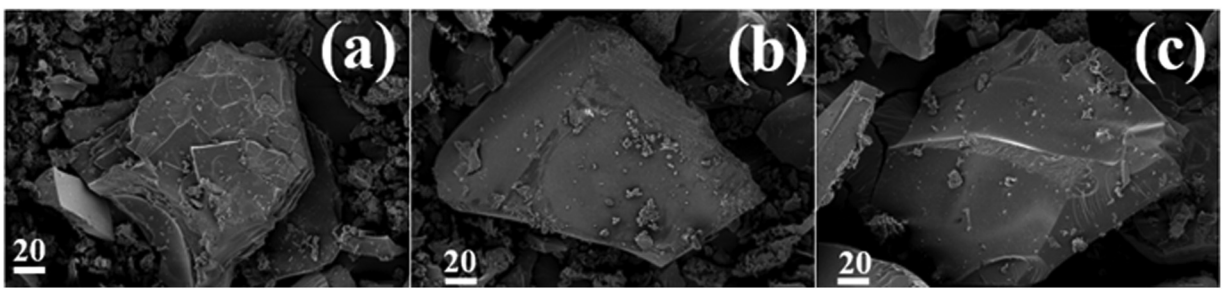

Fig. 2 SEM images of the CTFs: (a) CTFTTF@1-400, (b) CTFTTF@2-400, (c) CTFTTF@2-700. The length of the scale bar is given in μm.

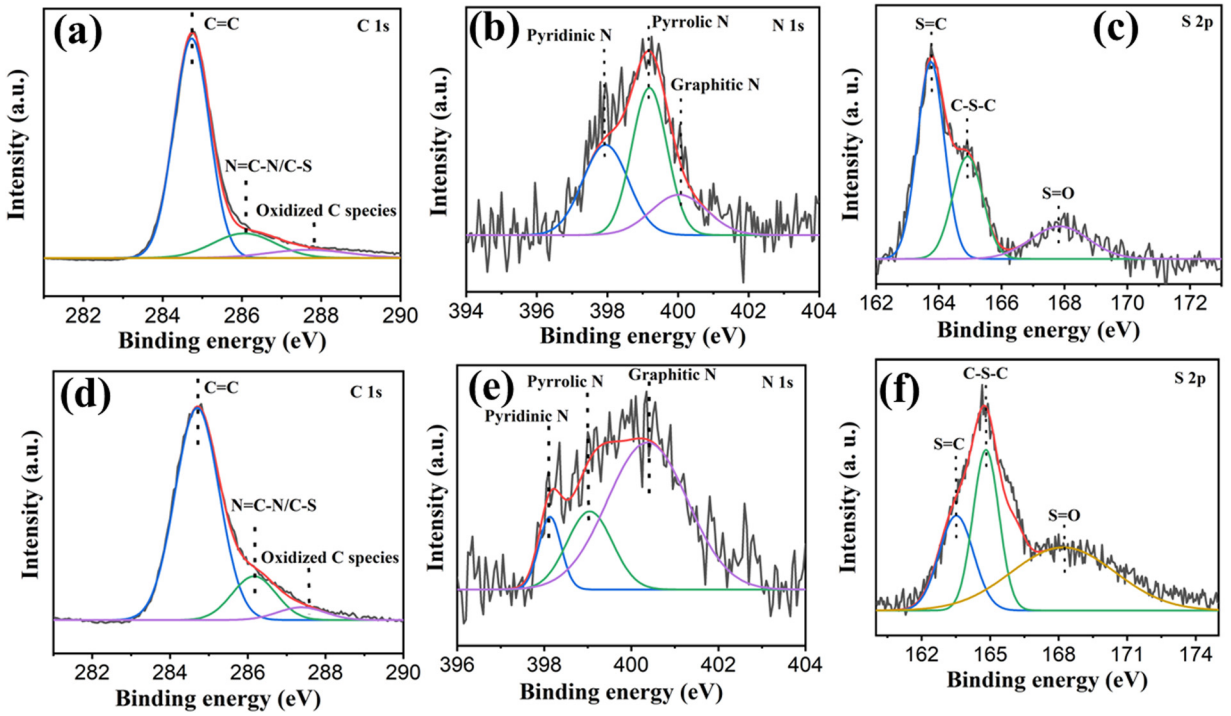

Fig. 3 (a) C 1s XPS of CTFTTF@2-400. (b) N 1s XPS of CTFTTF@2-400. (c) S 2p XPS of CTFTTF@2-400. (d) C 1s XPS of CTFTTF@2-700. (e) N 1s XPS of CTFTTF@2-700. (f) S 2p XPS of CTFTTF@2-700.

increased, the proportion of graphitic nitrogen in CTFTTFs has progressively increased as well (Table S2 in ESI†). To investigate whether the triazine ring is intact in CTFTTF@2-700, we performed solid-state ^{13}C CP/MAS NMR spectroscopy. As reported previously for other CTF materials, a broad hump was observed for CTFTTF@2-700, ranging from 100 to 160 ppm, lacking distinct structural features (Fig. S8 in ESI†).[21,45] Additionally, elemental analysis was performed to provide a clearer insight into the degree of degradation of the CTFTTFs as a function of temperature. It was observed that the nitrogen and sulfur content in all the obtained CTFs was significantly lower than the theoretically expected values (Table S1, ESI†). This can be attributed not only to the elimination of nitrogen and sulfur during the polymerization reaction but also to the possible entrapment of metal salts and water in the pores, which is consistent with findings from previous studies.[46]

The distinctive S,N-heteroatom-based framework, along with the high surface area and microporous characteristics of the prepared CTF materials, prompted us to further investigate their supercapacitor performance. To this end, CV tests were conducted on the synthesized CTF materials using a three-electrode system with a 1 mol L^{-1} Na_2SO_4 aqueous electrolyte at a scan rate of 10 mV s^{-1}. The resulting CV curves exhibited a quasi-rectangular shape, indicative of their capacitive and conductive properties (Fig. 4a).[13] The shape of the CV curve is characteristic of typical electrochemical double-layer capacitor behaviour and it is due to electrostatic interaction between the ions of electrolytes and the electrode interface. The XPS studies indicated that the prepared materials contain different types of nitrogen (pyridinic-type nitrogen, pyrrolic-type nitrogen and quaternary-type nitrogen) and sulphur (oxidized and unoxidized

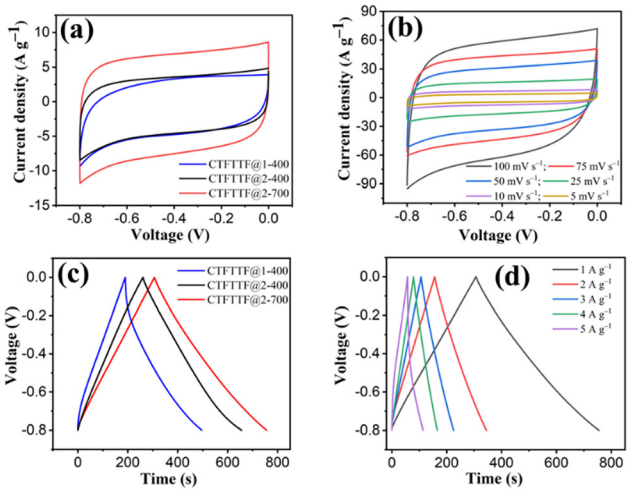

Fig. 4 (a) CV curve of CTFs, (b) CV curve of CTFTTF@2-700, (c) GCD curve of CTFs, and (d) GCD curve of CTFTTF@2-700.

species) atoms which provide a more polarized surface under an applied electric field. This surface enhances the electrostatic interaction between the ions of the electrolytes and the electrode interface. Among the three CTFs, CTFTTF@2-700 demonstrated the largest enclosed area under the CV curve, signifying the highest capacitance. Subsequently, CV measurements were taken at varying scan rates from 5 mV s^{-1} to 100 mV s^{-1}. The resulting profiles consistently exhibited a quasi-rectangular shape, further suggesting their excellent rate capability (Fig. 4b).[21] This finding prompted us to evaluate the charge storage characteristics of the three synthesized CTFs. The galvanostatic charge–discharge (GCD)

curves were recorded for these CTFs as depicted in Fig. 4c. For all CTFs, a triangular shape was observed in the GCD curves, indicating characteristic capacitive behavior. Notably, CTFTTF@2-700 exhibited a longer discharge time compared to the other two CTFs.

Moreover, we calculated the capacitance values from the GCD profiles using equation 2 (see the Experimental section) at the current density of 1 A g^{-1}. The specific capacitance values were found to be in the range of 630 F g^{-1} to 943 F g^{-1}. The specific capacitance of 943 F g^{-1} in three-electrode system for CTFTTF@2-700 beats previously reported values for other CTFs, such as p-CTF-800 (400 F g^{-1} at 1 A g^{-1}),[47] BPY-CTF (393.6 F g^{-1} at 0.5 A g^{-1}),[48] TCNQ-CTF (380 F g^{-1} at 1 A g^{-1}),[49] CTF-800 (628 F g^{-1} at 1 A g^{-1}),[13] pyrrolo[3,2-*b*]pyrrole-based CTF (638 F g^{-1} at 1 A g^{-1}),[50] and others (Table S3 in the ESI†). This comparison revealed that CTFTTF@2-700 showed the highest value of specific capacitance in the field of CTFs and CTF-derived materials. This exceptional capacitive performance of CTFTTF@2-700 can be attributed to a higher proportion of heteroatoms (nitrogen and sulfur) in the carbon material, a high specific surface area, and an inherent microporosity of the CTF-derived material. An increase in temperature from 400 °C to 700 °C resulted in the decomposition of triazine moieties in CTF and thereby, a higher percentage of graphitic nitrogen was detected for CTFTTF@2-700 in quantitative XPS analysis (Table S2, ESI†). Furthermore, GCD profile measurements were conducted at varying current densities ranging from 1 to 5 A g^{-1} (Fig. 4d). The consistently triangular shapes observed indicate a strong rate capability. Furthermore, the CV and GCD curves of these CTF materials have also been examined using different electrolytes including an alkali (KOH) and acid medium (H_2SO_4) in the negative potential window spanning from −0.8 V to 0 V (Fig. S10–S13, ESI†). The specific capacitance was calculated in the range of 382–517 F g^{-1} at 1 A g^{-1} using 1 M KOH medium, which is lower compared to CTFTTF@2-700 in 1 M Na_2SO_4. On the other hand, the CV and GCD measurements conducted in H_2SO_4 electrolyte often exhibit deviations from ideal capacitive behavior, primarily attributed to gas evolution (Fig. S10–S13, ESI†). A detailed analysis of the electrode process mechanism was carried out through electrochemical impedance spectroscopy (EIS), which is typically utilized to examine the charge storage processes in supercapacitors. A linear trend in the Nyquist plot indicated pure capacitive behaviour of all three materials (Fig. 5b). Notably, in the EIS of CTFTTF@2-700, the vertical line is nearly parallel to the imaginary impedance axis (*Y*-axis) even in the high frequency region.[50,51] In contrast, a greater deviation was observed for CTFTTF@1-400 and CTFTTF@2-400. These results are indicative of higher charge mobility throughout the working electrode made of CTFTTF@2-700, when compared to CTFTTF@1-400 and CTFTTF@2-400. Furthermore, the equivalent circuit depicted in Fig. 5b was constructed to fit the EIS data.[2,52,53] The charge-transfer resistances (R_{CT}) obtained from the fits are as follows: 21.43 Ω for CTFTTF@1-400, 18.23 Ω for CTFTTF@2-400, and 10.28 Ω for CTFTTF@2-700. These results indicate that CTFTTF@2-700 demonstrates a faster electron transfer rate compared to CTFTTF@1-400 and CTFTTF@2-400. Moreover,

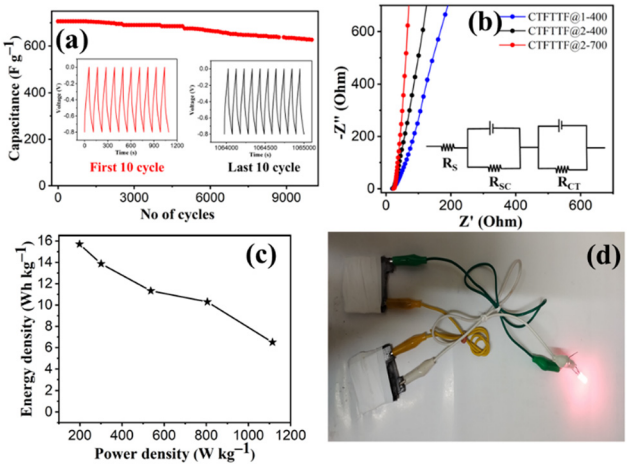

Fig. 5 (a) Cyclic retention of CTFTTF@2-700. (b) EIS of CTFTTFs. (c) Ragone plot of CTFTTF@2-700. (d) Lighting of a 1.8 V LED using CTFTTF@2-700.

the conductivity of the CTF materials was calculated through the current–voltage (*I*–*V*) measurement in the bias voltage range of ±2 V at room temperature (Fig. S14, ESI†). Among these devices, CTFTTF@2-700 showed higher conductivity (6.4 × 10^{-4} S cm^{-1}) than CTFTTF@2-400 (1.3 × 10^{-5} S cm^{-1}), and CTFTTF@1-400 (9.0 × 10^{-6} S cm^{-1}) and it is due to higher graphitic nitrogen content present in CTFTTF@2-700.[54] (Table S4, ESI†). The supercapacitive performance of CTFTTF@2-700 was further assessed using two-electrode symmetric supercapacitor devices with aqueous 1 mol L^{-1} Na_2SO_4 electrolyte. The CV and GCD tests were conducted on this device at various scan rates and current densities, respectively (Fig. S9a and b, ESI†). The device exhibited the specific capacitance of 708 F g^{-1} at a current density of 1 A g^{-1} in a two-electrode system. Moreover, the energy storage performance of a supercapacitor is primarily described by two fundamental parameters: energy density (*E*) and power density (*P*). According to the Ragone plot, the CTFTTF@2-700 device demonstrated an energy density of 15.7 W h kg^{-1} at a power density of 198 W kg^{-1}, and it achieved 6.5 W h kg^{-1} even at a high power density of 1125 W kg^{-1} (Fig. 5c) in a two-electrode system. The comparison table of power density for porous organic frameworks in aqueous media is provided in Table S5 (ESI†). Additionally, CTFTTF@2-700 demonstrated outstanding cycling stability, as it maintained its specific capacitance without significant degradation following 10 000 cycles at a current density of 5 A g^{-1}. The retention of specific capacitance of CTFTTF@2-700 was assessed at 90.5%, after 10 000 cycles validating its use as a high-quality nitrogen-functionalized CTF electrode for energy storage device (Fig. 5a). To provide a clearer perspective, the first and last 10 GCD cycles of the CTFTTF@2-700 samples are presented (Fig. 5a, inserted). To demonstrate a practical application, a photograph of a symmetric supercapacitor using Na_2SO_4 electrolyte was provided (Fig. 5d and Fig. S9d in the ESI†). Impressively, this supercapacitor was capable of powering a red 1.8 V light-emitting diode (LED), highlighting its practical utility in real-world scenarios.

Conclusions

In conclusion, we have investigated the supercapacitor performance of a series of sulfur heteroatom-functionalized porous CTF materials synthesized from 2,3,6,7-tetra(4-cyanophenyl)tetrathiafulvalene (TTFCN), a novel redox-active thiafulvalene-based monomer under ionothermal conditions. The effect of several synthesis parameters, such as monomer to $ZnCl_2$ ratio, reaction temperature and time on the microporosity, heteroatom content and the consequent microporosity and heteroatom enhanced supercapacitive performance of the synthesized materials were examined in detail. An exceptional specific capacitance value of 943 F g^{-1} was obtained for the CTF-derived carbon material CTFTTF@2-700, due to a mixed heteroatom (S and N) effect, a high specific surface area, and intrinsic microporosity of the synthesized material. This value stands as one of the highest among all CTFs synthesized under similar reaction conditions. Additionally, experiments conducted with a two-electrode symmetric supercapacitor device in aqueous electrolyte solution exhibited a specific capacitance of 708 F g^{-1} at 1 A g^{-1}, and an energy density of 15.7 W h kg^{-1} within a cell voltage of 0–0.8 V. We believe that the incorporation of heteroatoms (*e.g.*, sulfur and nitrogen) together with the ratio of micropores to mesopores are crucial for the development of new CTF materials for use in supercapacitor applications.

Author contributions

The manuscript was written through the contributions of all authors. All authors have given approval to the final version of the manuscript.

Data availability

We, the authors of this article, assure that the data will be provided upon reasonable request.

Conflicts of interest

There are no conflicts to declare.

Acknowledgements

This study was funded by SERB (EEQ/2020/000357), and a start-up grant from the UGC (No. F. 30-552/2021(BSR)). A. J. and A. M. acknowledge CSIR and UGC for the fellowship. We gratefully acknowledge Dr P. Lama for his valuable support with the SEM measurements.

References

1 K. Zhu, Z. Sun, Z. Li, P. Liu, H. Li and L. Jiao, *Adv. Energy Mater.*, 2023, **13**, 2203708.
2 C.-Y. Wang, T. Liu, X.-G. Yang, S. Ge, N. V. Stanley, E. S. Rountree, Y. Leng and B. D. McCarthy, *Nature*, 2022, **611**, 485–490.
3 Z. Pan, S. Yu, L. Wang, C. Li, F. Meng, N. Wang, S. Zhou, Y. Xiong, Z. Wang, Y. Wu, X. Liu, B. Fang and Y. Zhang, *Nanomaterials*, 2023, **13**, 1744.
4 S. Ghosh, S. Barg, S. M. Jeong and K. Ostrikov, *Adv. Energy Mater.*, 2020, **10**, 2001239.
5 G. Wang, L. Zhang and J. Zhang, *Chem. Soc. Rev.*, 2012, **41**, 797–828.
6 Y. Peng, Z. Chen, J. Wen, Q. Xiao, D. Weng, S. He, H. Geng and Y. Lu, *Nano Res.*, 2011, **4**, 216–225.
7 A. M. Khattak, H. Yin, Z. A. Ghazi, B. Liang, A. Iqbal, N. A. Khan, Y. Gao, L. Li and Z. Tang, *RSC Adv.*, 2016, **6**, 58994–59000.
8 S. Suriyakumar, P. Bhardwaj, A. N. Grace and M. A. Stephan, *Batteries Supercaps*, 2021, **4**, 571–584.
9 Y. Liao, H. Wang, M. Zhu and A. Thomas, *Adv. Mater.*, 2018, **30**, 1705710.
10 J. Y. Hwang, M. P. Li, M. F. El-Kady and R. B. Kaner, *Adv. Funct. Mater.*, 2017, **27**, 1605745.
11 L. Feng, K. Wang, X. Zhang, X. Sun, C. Li, X. Ge and Y. Ma, *Adv. Funct. Mater.*, 2018, **28**, 1704463.
12 H. An, Y. Li, P. Long, Y. Gao, C. Qin, C. Cao, Y. Feng and W. Feng, *J. Power Sources*, 2016, **312**, 146–155.
13 M. M. Vadiyar, X. Liu and Z. Ye, *ACS Appl. Mater. Interfaces*, 2019, **11**, 45805.
14 C. Zhu, Y. Liu, H. Zhang, H. Yang, X. Yin, Z. Li and X. Ma, *Int. J. Energy Res.*, 2021, **45**, 10963–10973.
15 S. Y. Lu, M. Jin, Y. Zhang, Y. B. Niu, J. C. Gao and C.-M. Li, *Adv. Energy Mater.*, 2017, **8**, 1702545.
16 Y.-F. Zhang, C.-M. Han, C. Bai, J.-J. Ma, L. Yu, L.-J. Sun, X.-Y. Zhang and H.-M. Hu, *ACS Appl. Nano Mater.*, 2024, **7**, 3897–3906.
17 M. G. Mohamed, S. V. Chaganti, S. U. Sharma, M. M. Samy, M. Ejaz, J.-T. Lee, K. Zhang and S.-W. Kuo, *ACS Appl. Energy Mater.*, 2022, **5**, 10130–10140.
18 P. Xiong, S. Zhang, R. Wang, L. Zhang, Q. Ma, X. Ren, Y. Gao, Z. Wang, Z. Guo and C. Zhang, *Energy Environ. Sci.*, 2023, **16**, 3181–3213.
19 C. Wu, H. Zhang, M. Hu, G. Shan, J. Gao, J. Liu, X. Zhou and J. Yang, *Adv. Electron. Mater.*, 2020, **6**, 2000253.
20 M. G. Mohamed, A. F. M. EL-Mahdy, M. M. M. Ahmed and S.-W. Kuo, *ChemPlusChem*, 2019, **84**, 1767–1774.
21 A. Maity, M. Siebels, A. Jana, M. Eswaran, R. Dhanusuraman, C. Janiak and A. Bhunia, *ChemSusChem*, 2024, **18**, e202401716, DOI: 10.1002/cssc.202401716.
22 M. Roy, B. Mishra, S. Maji, A. Sinha, S. Dutta, S. Mondal, A. Banerjee, P. Pachfule and D. Adhikari, *Angew. Chem., Int. Ed.*, 2024, **63**, e202410300.
23 C. Weng, X. Li, Z. Yang, H. Long, C. Lu, L. Dong, Z. Shuo and L. Tan, *Chem. Commun.*, 2022, **58**, 6809–6812.
24 L. Li, F. Lu, H. Guo and W. Yang, *Microporous Mesoporous Mater.*, 2021, **312**, 110766.
25 L. Rademacher, T. H. Y. Beglau, B. Ali, L. Sondermann, T. Strothmann, I. Boldog, J. Barthel and C. Janiak, *J. Mater. Chem. A*, 2024, **12**, 2093–2109.

26 P. Kuhn, M. Antonietti and A. Thomas, *Angew. Chem., Int. Ed.*, 2008, **47**, 3450–3453.
27 A. Bhunia, V. Vasylyeva and C. Janiak, *Chem. Commun.*, 2013, **49**, 3961–3963.
28 P. Kuhn, A. Forge, D. Su, A. Thomas and M. Antonietti, *J. Am. Chem. Soc.*, 2008, **130**, 13333–13337.
29 A. Jana, A. Maity, A. Sarkar, B. Show, P. A. Bhobe and A. Bhunia, *J. Mater. Chem. A*, 2024, **12**, 5244–5253.
30 A. Bhunia, I. Boldog, A. Möller and C. Janiak, *J. Mater. Chem. A*, 2013, **1**, 14990–14999.
31 S.-Y. Yu, J. Mahmood, H.-J. Noh, J.-M. Seo, S.-M. Jung, S.-H. Shin, Y.-K. Im, I.-Y. Jeon and J.-B. Baek, *Angew. Chem., Int. Ed.*, 2018, **57**, 8438–8442.
32 K. Park, K. Lee, H. Kim, V. Ganesan, K. Cho, S. K. Jeong and S. Yoon, *J. Mater. Chem. A*, 2017, **5**, 8576–8582.
33 A. Hryniewicka, J. Breczko, G. Siemiaszko, K. Brzezinski, A. Ilnicka, A. P. Terzyk and M. E. Plonska-Brzezinska, *Mater. Adv.*, 2024, **5**, 1065–1077.
34 J. Ren, H. Weng, B. Li, F. Chen, J. Liu and Z. S. Zhimin, *Front. Earth*, 2022, **10**, 841353.
35 S. Dey, A. Bhunia, I. Boldog, A. Möller and C. Janiak, *Microporous Mesoporous Mater.*, 2017, **241**, 303–315.
36 S. Li, T. Xing, Y. Wang, P. Lu, W. Kong, S. Li, X. Su and X. Wei, *Energy Res.*, 2021, **9**, 680761.
37 S. Dey, A. Bhunia, H. Breitzke, B. P. Groszewicz, G. Buntkowsky and C. Janiak, *J. Mater. Chem. A*, 2017, **5**, 3609.
38 K. S. Song, T. Ashirov, S. N. Talapaneni, A.-H. Clark, A. V. Yakimov, M. Nachtegaal, C. Copert and A. Coskun, *Chem*, 2022, **8**, 2043–2059.
39 G. Zhao, C. Chen, D. Yu, L. Sun, C. Yang, H. Zhang, Y. Sun, F. Besenbacher and M. Yu, *Nano Energy*, 2018, **47**, 547–555.
40 Y. Li, S. Zheng, X. Liu, P. Li, L. Sun, R. Yang, S. Wang, Z.-S. Wu, X. Bao and W.-Q. Deng, *Angew. Chem., Int. Ed.*, 2017, **57**, 7992–7996.
41 L. Hao, J. Ning, B. Luo, B. Wang, Y. Zhang, Z. Tang, J. Yang, A. Thomas and L. Zhi, *J. Am. Chem. Soc.*, 2015, **137**, 219–225.
42 Y. Li, G. Wang, T. Wei, Z. Fan and P. Yan, *Nano Energy*, 2016, **19**, 165–175.
43 Y. Zhao, K. X. Yao, B. Teng, T. Zhang and Y. Han, *Energy Environ. Sci.*, 2013, **6**, 3684.
44 S.-Y. Yu, J. Mahmood, H.-J. Noh, J.-M. Seo, S.-M. Jung, S.-H. Shin, Y.-K. Im, I.-Y. Jeon and J.-B. Baek, *Angew. Chem., Int. Ed.*, 2018, **57**, 8438–8442.
45 Y. Yusran, H. Li, X. Guan, D. Li, L. Tang, M. Xue, Z. Zhuang, Y. Yan, V. Valtchev, S. Qiu and Q. Fang, *Adv. Mater.*, 2020, **32**, 1907289.
46 G. Wang, K. Leus, S. Zhao and P. Van Der Voort, *ACS Appl. Mater. Interfaces*, 2018, **10**, 1244–1245; H. S. Jena, C. Krishnaraj, J. Schmidt, K. Leus, K. Van Hecke and P. Van Der Voort, *Chem. – Eur. J.*, 2020, **26**, 1437.
47 C. Wu, H. Zhang, M. Hu, G. Shan, J. Gao, J. Liu, X. Zhou and J. Yang, *Adv. Electron. Mater.*, 2020, **6**, 2000253.
48 Y. Zhang, B. Zhang, L. Chen, T. Wang, M. Di, F. Jiang, X. Xu and S. Qiao, *J. Colloid Interface Sci.*, 2022, **606**, 1534–1542.
49 Y. Li, S. Zheng, X. Liu, P. Li, L. Sun, R. Yang, S. Wang, Z. S. Wu, X. Bao and W. Q. Deng, *Angew. Chem., Int. Ed.*, 2017, **57**, 7992–7996.
50 A. Hryniewicka, J. Breczko, G. Siemiaszko, A. N. Papathanassiou, K.-G. Marek, K. A. Tarach, K. Brzezinski, A. Ilnicka, A. P. Terzyk, K. H. Markiewicz, L. Echegoyen and M. E. Plonska-Brzezinska, *Sci. Rep.*, 2023, **13**, 10737.
51 T. S. Mathis, N. Kurra, X. Wang, D. Pinto, P. Simon and Y. Gogotsi, *Adv. Energy Mater.*, 2019, **9**, 1902007.
52 S. R. Hastak, P. Sivaraman, D. D. Potphode, K. Shashidhara and B.-A. Samui, *Electrochim. Acta*, 2012, **59**, 296–303.
53 X. Bu, G. Wang and Y. Tian, *Nanoscale*, 2017, **9**, 17513–17523.
54 Y. Li, S. Zheng, X. Liu, P. Li, L. Sun, R. Yang, S. Wang, Z.-S. Wu, X. Bao and W.-Q. Deng, *Angew. Chem., Int. Ed.*, 2018, **57**, 7992–7996.